

A statistical approach for isolating fossil fuel emissions in atmospheric inverse problems

Vineet Yadav^{1#}, Anna M. Michalak², Jaideep Ray³ and Yoichi P. Shiga^{2, 4}

[1] Jet Propulsion Laboratory, California Institute of Technology, Pasadena, California, USA
94305

[2] Department of Global Ecology, Carnegie Institution for Science, Stanford, California

[3] Sandia National Laboratories, Livermore, California

[4] Department of Civil and Environmental Engineering, Stanford University, Stanford, California

Correspondence to: Vineet Yadav (vineet.yadav@jpl.nasa.gov)

1 **Abstract**

2 Independent verification and quantification of fossil fuel (FF) emissions constitutes a considerable
3 scientific challenge. By coupling atmospheric observations of CO₂ with models of atmospheric
4 transport, inverse models offer the possibility of overcoming this challenge. However,
5 disaggregating the biospheric and FF flux components of terrestrial fluxes from CO₂ concentration
6 measurements has proven to be difficult, due to observational and modeling limitations. In this
7 study, we propose a statistical inverse modeling scheme for disaggregating winter-time fluxes on
8 the basis of their unique error covariances and covariates, where these covariances and covariates
9 are representative of the underlying processes affecting FF and biospheric fluxes. The application
10 of the method is demonstrated with one synthetic and two real data prototypical inversions by
11 using in-situ CO₂ measurements over North America. Inversions are performed only for the month
12 of January, as predominance of biospheric CO₂ signal relative to FF CO₂ signal and observational
13 limitations, preclude disaggregation of the fluxes in other months. The quality of disaggregation
14 is assessed primarily through examination of a posteriori covariance between disaggregated FF
15 and biospheric fluxes at regional scales. Findings indicate that the proposed method is able to
16 robustly disaggregate fluxes regionally at monthly temporal resolution with a posteriori cross-
17 covariance lower than 0.15 μmol m⁻² sec⁻¹ between FF and biospheric fluxes. Error covariance
18 models and covariates based on temporally varying FF inventory data provide a more robust
19 disaggregation over static proxies (e.g., nightlight intensity, population density). However, the
20 synthetic data case study shows that disaggregation is possible even in absence of detailed
21 temporally varying FF inventory data.

22 1 Introduction

23 The rising concentration of carbon dioxide (CO₂) in the atmosphere is the main driver of
24 anthropogenic climate change. Spatial and temporal variations in global CO₂ fluxes leading to this
25 increase can be inferred using inverse models from atmospheric observations that reflect the
26 combined influence of fossil fuel (FF), biospheric, and oceanic fluxes. In inverse models, CO₂
27 concentration measurements are combined with atmospheric transport models driven by observed
28 meteorology to yield estimates of the net exchange of CO₂ at the land and ocean surface [e.g.,
29 *Gurney et al.*, 2002; *Michalak et al.*, 2004; *Rayner et al.*, 1999; *Tans et al.*, 1990].

30 Recently, atmospheric inverse models have been proposed as a potential tool for independent
31 verification of inventory-based estimates of FF fluxes or emissions. Such applications currently
32 do not exist at regional (e.g. 1° by 1° and sub-monthly scale) to continental scales, due to the
33 limitations associated with observational coverage [*Pacala et al.*, 2010]. Improvements in terms
34 of increasing in-situ [e.g., *Sloop and Novakovskaia*, 2012] and satellite measurements [e.g., *Duren*
35 *and Miller*, 2012] of CO₂ concentrations and in-situ measurements of radiocarbon isotope ¹⁴C
36 [*Miller et al.*, 2012] have been suggested as options towards reducing the uncertainty associated
37 with continental and regional FF emissions estimates.

38 A variety of targeted efforts are ongoing for FF flux estimation at local to urban scales. Examples
39 focusing on urban areas include the Megacities Carbon Project [*Duren and Miller*, 2012; *Kevin R.*
40 *Gurney et al.*, 2012; *Kort et al.*, 2012] and the Indianapolis Flux Experiment (INFLUX)
41 (<http://influx.psu.edu/>). At local scales [0.2-5 Kms; *Christen*, 2014] the eddy covariance method has
42 been employed to quantify FF emissions upwind from the location of the measurement tower
43 [*Matese et al.*, 2009; *Newman et al.*, 2008; *Velazco et al.*, 2011]. Estimation of FF fluxes and

44 identification of its sources have also been attempted by studying upwind and downwind
45 differences in the CO₂ mixing ratios along transects in urban and/or rural areas [*George et al.*, 2007;
46 *Gratani and Varone*, 2005; *Idso et al.*, 2001; *Mays et al.*, 2009; *Rice and Bostrom*, 2011; *Rigby et al.*,
47 2008]. Other urban studies have represented urban areas as boxes [*McKain et al*, 2014; *Kort et al*,
48 2012; *Turnbull et al*, 2011] with well-mixed boundary layer [see; *Newman et al.*, 2008; *Reid and*
49 *Steyn*, 1997; *Strong et al.*, 2011], whose height is determined by scattering of sound waves [e.g.,
50 *Zimnoch et al.* 2010] or through tracers like radon [e.g., *Vogel et al.*, 2013] and fluxes are estimated
51 by accounting for differences in upwind and downwind CO₂ concentrations [*Lauvaux et al.*, 2013].
52 However, all these methods are extremely sensitive to the characterization of background
53 concentrations, wind speed, boundary layer and urban heat island [for details see; *Cambaliza et al.*,
54 2013]. Moreover these methods do not scale to national or continental scales, and can typically
55 only be used to validate FF fluxes in urban areas.

56 Estimation of FF fluxes from inverse methods at continental scales requires disaggregation of
57 biospheric and FF fluxes which has proven to be difficult due to seasonal variations in the
58 contribution of these fluxes in determining total surface flux of CO₂ (*Shiga et al.* 2014). Remote
59 sensing of CO₂ has the capability to provide a large number of observations [for discussion on
60 CO₂ observations from space see; *Crisp et al.*, 2004; *Olsen et. al.*, 2004] that can reduce the
61 uncertainty of the FF fluxes estimated within an inverse modeling framework.

62 However, beyond an increase in observations, methodological improvements are also required in
63 both transport and inverse models to realize the full potential of current and future CO₂
64 observations. In the case of inverse models, these methodological improvements include designing

65 inverse modeling approaches that leverage the distinct statistical signatures of FF and biospheric
66 fluxes in order to pinpoint their contributions to the total surface flux of CO₂.

67 To date, inversion efforts aimed at separating FF emissions from biospheric fluxes have relied on
68 the use of isotopic tracers of FF CO₂ emissions [e.g., *Brioude et al.*, 2012;] to identify its
69 contribution to the total CO₂ signal [for details on tracers of FF CO₂ see *Miller et al.*, 2012].
70 However, a large fraction of the variance in FF fluxes remains unexplained by these tracers [*Miller*
71 *et al.*, 2012]. Studies that address the estimation of FF emissions over large spatial regions
72 (compared to urban domes) are rare. In Ray et al. (2014a), the authors developed a
73 parameterization of FF emission fields based on wavelets, and in Ray et al. (2014b) they use a
74 sparse reconstruction method to estimate FF emissions using their spatial model in a synthetic data
75 test case. Those methods were only applied within synthetic data experiments, however, and did
76 not address the need to isolate FF emissions in the presence of biospheric fluxes. A study by Shiga
77 et al. (2014), although not an inversion study per se, examined the degree to which concentration
78 signatures specific to FF emissions were discernable from biospheric fluxes given (1) the current
79 state of the atmospheric monitoring network in North America, (2) co-variations between the
80 seasonalities of variability in fluxes and atmospheric transport, and (3) limitations associated with
81 contemporary atmospheric transport models. They found that outside of winter months, space-time
82 patterns specific to FF emissions could not even be conclusively detected in observations of CO₂
83 from the North American monitoring network.

84 Here, we hypothesize that, for times and regions where the atmospheric monitoring network and
85 atmospheric transport model provide, at a minimum, sufficient information to detect FF emissions,
86 one could use the unique spatiotemporal features of FF fluxes to isolate them from confounding

87 biospheric fluxes. To explore this idea, we present a geostatistical inverse modeling methodology
88 that does not rely on FF tracers to separate FF and biospheric fluxes. Rather, the approach relies
89 on (1) identifying spatially- and temporally-explicit covariates (variables correlated with FF
90 emissions like night lights, population density among others) that provide some information about
91 the space-time patterns of FF emissions, and (2) isolating the covariance structure of the portion
92 of the FF emissions patterns that cannot be captured by these covariates. A similar idea is applied
93 to biospheric fluxes, with covariates and a covariance structure unique to the biospheric component
94 of the total flux signal. Specifically, we treat easily-observed proxies of FF and biospheric CO₂
95 fluxes as a continuous predictors to construct a linear model for them; the models are then used
96 within a geostatistical inverse formulation (e.g. Michalak et al. 2004; Gourdji et al. 2012; Fang et
97 al. 2015). The applicability of the proposed method is demonstrated within the context of one
98 synthetic and two real data inversions at 1° spatial resolution for North America for the month of
99 January 2008. In the synthetic data case study true fluxes are known in advance and are used to
100 generate pseudo measurements. These measurements are then used to estimate fluxes. This allows
101 direct comparison of the spatial distribution and magnitude of the true and estimated fluxes which
102 is not possible in the real data case studies where true fluxes remain unknown.

103 The month of January is selected based on the analysis in Shiga et al. (2014) and the need to focus
104 on a time when FF emissions are, at a minimum, detected given the limitations of the in-situ
105 monitoring network present in 2008 and atmospheric transport models. In these inversions the
106 covariates and the error covariance model for biospheric fluxes are prescribed, whereas covariates
107 and error covariance model for FF fluxes are chosen from a set of candidate covariates and error
108 covariance models.

109 For more extensive applications, a method such as the one proposed here would need to be coupled
110 with more widespread observational coverage provided by satellites and in-situ measurement
111 network, and ideally with improved atmospheric transport models.

112 **2 Method for flux disaggregation**

113 The process of disaggregating CO₂ fluxes is completed in two steps. First, the error covariance
114 model and covariates for FF fluxes are selected using Bayesian Information Criterion (BIC; see
115 section 2.4) and Restricted Maximum Likelihood (RML; see section 2.4) within geostatistical
116 inverse modeling framework, after which in the second step, geostatistical inversions for
117 separating FF and biospheric fluxes (see section 2.5.) are conducted. The quality of the separation
118 of CO₂ fluxes is assessed, by examining a posteriori cross-covariances between FF and biospheric
119 fluxes.

120 **2.1 Geostatistical method for separating fossil fuel and biospheric fluxes**

121 A geostatistical formulation of the atmospheric inverse problem has been used to estimate
122 biospheric CO₂ fluxes in several earlier studies [e.g., *Gourdji et al.*, 2012; *Michalak et al.*, 2004].
123 Unlike other Bayesian methods, this approach does not rely on prescribing prior fluxes; instead,
124 it models the prior as a linear combination of a set of covariates with weights that are treated as
125 hyperparameters (β) and estimated as part of the inverse problem. Generally, covariates correlated
126 with the flux are chosen to model the prior mean [e.g., *Gourdji et al.*, 2008]. However, the approach
127 also allows for the inclusion of covariates that are output from inventories and/or process based
128 models [e.g., *Fang et al.*, 2014].

129 Under the assumption that the model-data mismatch can be modeled as a Gaussian distribution,
 130 the objective function for the standard geostatistical inverse model (GIM) can be written as:

$$L_{\mathbf{s},\boldsymbol{\beta}} = \frac{1}{2}(\mathbf{z} - \mathbf{H}\mathbf{s})^T \mathbf{R}^{-1}(\mathbf{z} - \mathbf{H}\mathbf{s}) + \frac{1}{2}(\mathbf{s} - \mathbf{X}\boldsymbol{\beta})^T \mathbf{Q}^{-1}(\mathbf{s} - \mathbf{X}\boldsymbol{\beta}) \quad (1)$$

131 where \mathbf{z} are measurements of CO₂ concentrations, \mathbf{H} is a Jacobian matrix representing the
 132 sensitivity of measurements to underlying flux, \mathbf{s} are the CO₂ fluxes, \mathbf{R} is the model-data mismatch
 133 error covariance matrix, \mathbf{X} is a matrix of covariates of \mathbf{s} , $\boldsymbol{\beta}$ are the coefficients or weights of
 134 individual covariates and \mathbf{Q} is the error covariance matrix describing the deviations of \mathbf{s} from $\mathbf{X}\boldsymbol{\beta}$.
 135 In this study, we modify this objective function to separately account for biospheric and FF fluxes.
 136 This modified objective function can be written as:

$$\begin{aligned} L_{\mathbf{s}_{bio},\mathbf{s}_{ff},\boldsymbol{\beta}_{bio},\boldsymbol{\beta}_{ff}} \\ &= \frac{1}{2}(\mathbf{z} - [\mathbf{H}_{bio}\mathbf{s}_{bio} + \mathbf{H}_{ff}\mathbf{s}_{ff}])^T \mathbf{R}^{-1}(\mathbf{z} - [\mathbf{H}_{bio}\mathbf{s}_{bio} + \mathbf{H}_{ff}\mathbf{s}_{ff}]) \\ &+ \frac{1}{2}(\mathbf{s}_{bio} - \mathbf{X}_{bio}\boldsymbol{\beta}_{bio})^T \mathbf{Q}_{bio}^{-1}(\mathbf{s}_{bio} - \mathbf{X}_{bio}\boldsymbol{\beta}_{bio}) \\ &+ \frac{1}{2}(\mathbf{s}_{ff} - \mathbf{X}_{ff}\boldsymbol{\beta}_{ff})^T \mathbf{Q}_{ff}^{-1}(\mathbf{s}_{ff} - \mathbf{X}_{ff}\boldsymbol{\beta}_{ff}) \end{aligned} \quad (2)$$

137 where the subscripts *bio* and *ff* represent the biospheric and FF component of the terms defined in
 138 equation 1. This modified objective function embodies the assumptions that suitable covariates (in
 139 \mathbf{X}) and error covariance models (\mathbf{Q}) can be defined to statistically isolate FF and biospheric fluxes.
 140 Thus, the covariates (\mathbf{X}_{bio} , \mathbf{X}_{ff}) and error covariance models (\mathbf{Q}_{bio} , \mathbf{Q}_{ff}) in equation 2 play a vital
 141 role, as they capture our understanding of the processes affecting FF and biospheric flux
 142 variability. \mathbf{H}_{bio} and \mathbf{H}_{ff} in this study are based on the same atmospheric transport model, but are

143 kept separate to allow for the possibility of modeling \mathbf{s}_{bio} and \mathbf{s}_{ff} at different spatiotemporal
144 resolutions.

145 The covariates and error covariance models in section 2.2 and 2.3 are discussed specifically in the
146 context of the three inversion case studies presented in this work. Other covariates and error
147 covariance models could be implemented within equation 2, as needed for other applications.

148 **2.2 Covariates and error covariance model for biospheric fluxes**

149 For the three inversion case studies presented here, the only covariates used for biospheric fluxes
150 in \mathbf{X}_{bio} are fixed effects that represent a 3-hourly diurnal cycle (see, section 3 for details on the
151 resolution of inversions). These covariates model the mean diurnal variations in the biospheric
152 fluxes, and any spatiotemporal deviations therefrom are captured by the error covariance matrix
153 \mathbf{Q}_{bio} . This choice of covariates for biospheric fluxes was made to focus primarily on evaluating
154 the proposed method's ability to represent FF emissions.

155 Biospheric fluxes vary relatively smoothly, exhibit spatial autocorrelation, and are largely
156 independent of FF fluxes. Thus, it is assumed for the inversion case studies that the error
157 covariance for biospheric fluxes can be modeled through a stationary [for definition of stationarity
158 see *Cressie*, 1993] spatio-temporal exponential covariance model [see *Gourdji et al.*, 2012]. This
159 error covariance model can be written as [for details see *Gourdji et al.*, 2010; *Yadav and Michalak*,
160 2013]:

$$\mathbf{Q}_{bio} = \sigma^2 \left[\exp\left(\frac{-\mathbf{h}_{temporal_{bio}}}{l_{temporal_{bio}}}\right) \otimes \exp\left(\frac{-\mathbf{h}_{spatial_{bio}}}{l_{spatial_{bio}}}\right) \right] \quad (3)$$

161 where σ^2 is the variance in space and time, $\mathbf{h}_{spatial_{bio}}$ and $\mathbf{h}_{temporal_{bio}}$, are the separation
162 distances between estimation locations of biospheric fluxes in space and time, and $l_{temporal_{bio}}$ and
163 $l_{spatial_{bio}}$ are the spatial and temporal correlation range parameters and \otimes denotes the Kronecker
164 product. The three parameters σ^2 , $l_{temporal_{bio}}$, $l_{spatial_{bio}}$ of the spatio-temporal error covariance
165 model are estimated through RML (see, section 2.4. for details)

166 **2.3 Covariates and error covariance model for fossil fuel fluxes**

167 To aid in the disaggregation of FF fluxes from the biospheric fluxes, we include covariates that
168 are correlated with FF fluxes in \mathbf{X}_{ff} . There are many easily available/observable proxies that
169 correlate with FF fluxes, and we use the BIC [Schwarz, 1978] to select the smallest, most
170 informative subset from a set of candidate proxies. This is described in detail in section 2.4. For
171 the inversions presented here, the superset of candidate covariates of FF fluxes includes (1) annual
172 radiance intensity of night lights at 3 km spatial resolution for 2008 [Elvidge *et al.*, 1997], (2)
173 annual population density per sq. km at ~ 5 km spatial resolution for 2008 [CIESIN, 2004], (3) %
174 built up area at ~10 km spatial resolution for 2002 [Miteva, 2002], (4) % urban area for 2009
175 [Schneider *et al.*, 2009], and (5) a mixed, scaled estimate of FF fluxes of North America for 2008
176 from Vulcan and ODIAC (see Section 3.1). All variables are aggregated up to the 1° spatial
177 resolution for inversions.

178 Any spatiotemporal deviations from $\mathbf{X}_{ff}\boldsymbol{\beta}_{ff}$ are assumed to be independent, and can thus be
179 represented through a diagonal error covariance matrix with a different variance for each spatial
180 location (i.e., each grid-cell). This is consistent with the fact that FF fluxes estimated at 1° spatial

181 resolution tend to be spatially localized (see section 3 for details on the spatial resolution of
182 inversions).

183 The FF error covariance is thus defined here as:

$$\mathbf{Q}_{ff} = \left(a \begin{bmatrix} k_1 & 0 & 0 \\ 0 & \ddots & 0 \\ 0 & 0 & k_r \end{bmatrix} + b \begin{bmatrix} 1 & 0 & 0 \\ 0 & \ddots & 0 \\ 0 & 0 & 1 \end{bmatrix} \right) \quad (4)$$

184 where a and b are constant variance components for all time periods for r spatial locations at which
185 FF fluxes are estimated, and k_1, \dots, k_r define additional error variance that is spatially independent
186 (i.e. the variance at each estimation location can be different).

187 We assume that the k_i 's in equation 4 can be prescribed based on geospatial datasets related to FF
188 fluxes, ten of which are considered here. The first nine are the mean, maximum and variance of
189 night lights, population density, and % built up area within each $1^\circ \times 1^\circ$ grid-cell in the inversion
190 domain. These can be defined because all three of these datasets are available at higher resolution
191 than the resolution of the inversions. The final dataset considered is a FF inventory (Vulcan
192 combined with ODIAC; see section 4) at the resolution of the inversions (see section 3 for details
193 on the resolution of inversions), with this final dataset being temporally, as well as spatially,
194 variable.

195 BIC is used to identify those geospatial datasets that most represent actual error covariances which
196 are then used to populate the k_i 's (see Section 2.3). The primary objective is to obtain an optimal
197 model that, in combination with covariates in \mathbf{X}_{ff} , can explain the spatiotemporal variability of FF
198 fluxes.

199 **2.4 Covariate and Covariance Selection from Bayesian Information Criterion**

200 BIC evaluates the tradeoff between the explanatory power of a model and its complexity. It is used
 201 for selecting an appropriate set of covariates from a superset of candidate covariates of the
 202 dependent variable. The set of covariates that forms the model with the lowest BIC value,
 203 optimally balances explanatory power with model complexity. In this study, BIC is used to select
 204 covariates for both \mathbf{X}_{ff} and \mathbf{Q}_{ff} . BIC is defined as:

$$BIC = \underbrace{RSS + \ln|\Psi|}_{\text{log likelihood}} + \underbrace{p \ln(n)}_{\text{penalty term}} \quad (5)$$

205 where $||$ denotes the matrix determinant, p are the number of parameters or covariates in the model
 206 and n is the number of observations.

207 RSS in equation 5 is defined as ,

$$RSS = [\mathbf{z}^T (\Psi^{-1} - \Psi^{-1} \Omega (\Omega^T \Psi^{-1} \Omega)^{-1} \Omega^T \Psi^{-1}) \mathbf{z}] \quad (6)$$

208 where

$$\Psi = [\mathbf{H}_{bio} \quad \mathbf{H}_{ff}] \begin{bmatrix} \mathbf{Q}_{bio} & \mathbf{0} \\ \mathbf{0} & \mathbf{Q}_{ff} \end{bmatrix} [\mathbf{H}_{bio} \quad \mathbf{H}_{ff}]^T + \mathbf{R} \quad (7)$$

209 and

$$\Omega = [\mathbf{H}_{bio} \quad \mathbf{H}_{ff}] \begin{bmatrix} \mathbf{X}_{bio} \\ \mathbf{X}_{ff} \end{bmatrix} \quad (8)$$

210 Note that BIC (eq. 5) depends on the covariance parameters in \mathbf{Q}_{ff} (i.e., a and b), \mathbf{Q}_{bio} (σ^2 ,
 211 $l_{temporal_{bio}}$ and $l_{spatial_{bio}}$) and \mathbf{R} (σ_R^2), which themselves depend on the covariates used to define

212 \mathbf{X}_{ff} and \mathbf{Q}_{ff} . The covariates and covariance parameters must therefore be adjusted in tandem to
 213 identify the overall best statistical model. We proceed as follows:

- 214 (1) Pick one of the ten covariates considered for populating the FF error covariance model
 215 (\mathbf{Q}_{ff} , eq. 4).
- 216 (2) Use the discrete optimization branch and bound algorithm [see *Yadav et al.*, 2013] and
 217 RML [for details see *Kitanidis*, 1995] to select covariates (\mathbf{X}_{ff}) and covariance parameters
 218 of \mathbf{Q}_{ff} , \mathbf{Q}_{bio} , and \mathbf{R} (for estimates of covariance parameters of \mathbf{Q}_{ff} , \mathbf{Q}_{bio} see Appendix 1
 219 and 3); to simultaneously minimize BIC and the log likelihood of the expected value of
 220 the measurements (\mathbf{z}) with respect to a choice of a covariance model of \mathbf{Q}_{ff} in step 1. This
 221 optimization procedure gives a set of covariates and covariance parameters associated with
 222 FF error covariance chosen in step 1.
- 223 (3) Repeat steps 1 and 2 for each of the ten different \mathbf{Q}_{ff} i.e., FF error covariance models
 224 described in section 2.3
- 225 (4) Compare BIC obtained in step 2 for all the ten FF error covariance models and select the
 226 error covariance model that results in the minimum BIC.

227 **2.5 Flux and a posteriori covariance estimation**

228 The FF and biospheric fluxes are estimated by solving linear system of equations 9 and 10 [e.g.,
 229 *Michalak et al.*, 2004], following which a posteriori covariance can be obtained from equation 11.

$$\begin{bmatrix} \boldsymbol{\Psi} & \boldsymbol{\Omega} \\ \boldsymbol{\Omega}^T & \mathbf{0} \end{bmatrix} \begin{bmatrix} [\boldsymbol{\Lambda}_{bio} & \boldsymbol{\Lambda}_{ff}]^T \\ \mathbf{M} \end{bmatrix} = \begin{bmatrix} [\mathbf{H}_{bio} & \mathbf{H}_{ff}] \begin{bmatrix} \mathbf{Q}_{bio} & \mathbf{0} \\ \mathbf{0} & \mathbf{Q}_{ff} \end{bmatrix} \\ \begin{bmatrix} \mathbf{X}_{bio} \\ \mathbf{X}_{ff} \end{bmatrix} \end{bmatrix} \quad (9)$$

$$\begin{bmatrix} \hat{\mathbf{S}}_{bio} \\ \hat{\mathbf{S}}_{ff} \end{bmatrix} = [\mathbf{\Lambda}_{bio} \quad \mathbf{\Lambda}_{ff}]^T \mathbf{z} \quad (10)$$

$$\mathbf{V} = - \begin{bmatrix} \mathbf{X}_{bio} \\ \mathbf{X}_{ff} \end{bmatrix} \mathbf{M} + \begin{bmatrix} \mathbf{Q}_{bio} & \mathbf{0} \\ \mathbf{0} & \mathbf{Q}_{ff} \end{bmatrix} - \begin{bmatrix} \mathbf{Q}_{bio} & \mathbf{0} \\ \mathbf{0} & \mathbf{Q}_{ff} \end{bmatrix} [\mathbf{H}_{bio} \quad \mathbf{H}_{ff}]^T [\mathbf{\Lambda}_{bio} \quad \mathbf{\Lambda}_{ff}]^T \quad (11)$$

230

231 In equations 9, 10 and 11, \mathbf{V} is the a posteriori covariance of the estimated fluxes $\hat{\mathbf{S}}_{bio}$ and $\hat{\mathbf{S}}_{ff}$,
 232 $\mathbf{\Lambda}_{bio}$ and $\mathbf{\Lambda}_{ff}$ are the matrix of weights, \mathbf{M} are lagrange multipliers, and the remaining terms are
 233 as defined earlier. The posterior covariance matrix \mathbf{V} in equation 11 can be subdivided to represent
 234 the posterior covariances of the biospheric and FF fluxes, as well as their cross-covariance, and
 235 can be given as:

$$\mathbf{V} = \begin{bmatrix} \mathbf{V}_{bio} & \mathbf{V}_{ff,bio}^T \\ \mathbf{V}_{ff,bio} & \mathbf{V}_{ff} \end{bmatrix}$$

237 where \mathbf{V}_{bio} , \mathbf{V}_{ff} represent posterior covariance of estimated biospheric and FF fluxes and $\mathbf{V}_{ff,bio}$
 238 represent their cross-covariance.

239 2.6 Non-Negativity constraints on fossil fuel fluxes

240 The joint inversion can result in negative FF fluxes, and therefore a non-negativity constraint is
 241 imposed on the FF fluxes obtained from equation 10. No constraints are imposed on $\hat{\mathbf{S}}_{bio}$, $\hat{\mathbf{\beta}}_{bio}$ and
 242 $\hat{\mathbf{\beta}}_{ff}$ as they admit both negative and positive values. There are several methods for imposing non-
 243 negativity constraints on $\hat{\mathbf{S}}_{ff}$ [e.g., *Miller et al.*, 2014]. However, some of these methods do not
 244 scale to large dimensional inverse problems while others make the problem nonlinear.
 245 Consequently, we used Lagrange multipliers as a mechanism for implementing the non-negativity

246 constraints. This method consists of rewriting the original objective function given in equation 2
 247 into a Lagrangian formulation [e.g., *Michalak and Kitanidis, 2003*]:

$$h(L_{\mathbf{s}_{bio}, \mathbf{s}_{ff}, \mathbf{\beta}_{bio}, \mathbf{\beta}_{ff}}, \boldsymbol{\lambda}) = f(L_{\mathbf{s}_{bio}, \mathbf{s}_{ff}, \mathbf{\beta}_{bio}, \mathbf{\beta}_{ff}}) - \sum_{i=1}^t \lambda_i [\delta_i(\mathbf{s}_{ff}) - b_i]$$

248 where t are the total number of active constraints, and $\boldsymbol{\lambda} = (\lambda_1, \lambda_1 \dots \lambda_p)$ are the Lagrange
 249 multipliers and $L_{\mathbf{s}_{bio}, \mathbf{s}_{ff}, \mathbf{\beta}_{bio}, \mathbf{\beta}_{ff}}$ must satisfy the constraints such that $\delta_i(\mathbf{s}_{ff}) \geq b_i$. This involves
 250 setting the derivative of the Lagrange function equal to zero by satisfying the first order Kuhn-
 251 Tucker conditions [for additional details see *Gill et al., 1981*]. Note that non-negativity constraints
 252 are imposed on FF fluxes obtained from an unconstrained inversion that utilizes the covariance
 253 model and covariates selected from the procedure described in section 2.4. While imposing non-
 254 negativity $\hat{\mathbf{s}}_{bio}$, $\hat{\mathbf{s}}_{ff}$, $\hat{\boldsymbol{\beta}}_{bio}$ and $\hat{\boldsymbol{\beta}}_{ff}$ are updated in each iteration, the a posteriori covariance is not
 255 updated and the uncertainty reported in section 5.3 is obtained from the first inversion where non-
 256 negativity constraints are not imposed.

257 **3 Inversion Case Studies**

258 Three inversion case studies are used to evaluate the proposed approach. All involve estimating
 259 biospheric fluxes at 3-hourly temporal resolution to avoid temporal aggregation errors [for details
 260 see *Gourdji et al., 2010*], while FF fluxes are estimated at 8-day temporal resolution, in part due
 261 to the computational cost of imposing non-negativity constraints. Spatially, both FF and biospheric
 262 fluxes are estimated at 1° by 1° for the land area between 10° N to 70° N and 50° W to 170° W.
 263 All inversions are conducted for January 2008.

264 3.1 Data for inversion case studies

265 The sensitivity matrix (\mathbf{H}) of the CO₂ observations to surface fluxes for inversions was obtained
266 from Weather Research Forecasting model-Stochastic Time-Inverted Lagrangian Transport
267 [STILT; *Lin et al.*, 2003] model that has been utilized in many studies for estimating fluxes [for
268 details see *Gourdji et al.*, 2012b; *Shiga et al.*, 2014].

269 For two real data case studies continuous measurements of atmospheric CO₂ concentrations from
270 29 in-situ towers across North America were used. These 29 towers include: (1) nine towers
271 operated by the Global Monitoring Division of NOAA's Earth Research Laboratory [Andrews et
272 al., 2014], located in Park Falls, Wisconsin (LEF), Moody, Texas (WKT), West Branch, Iowa
273 (WBI), Boulder Atmospheric Observatory, Colorado (BAO), Argyle, Maine (AMT), South
274 Carolina Tower, South Carolina (SCT) and Walnut Grove, California (WGC), Shenandoah
275 National Park, Virginia (SNP), and Barrow, Alaska (BRW) [*Thoning et al.*, 2014]; (2) seven
276 towers supported by the Mid-Continental Intensive project, located in Canaan Valley, West
277 Virginia (CVA), Missouri Ozarks, Missouri (OZA) [*Stephens et al.*, 2011], Kewanee, Illinois
278 (KEW), Centerville, Iowa (CEN), Mead, Nebraska (MEA), Round Lake, Missouri (ROL), and
279 Galesville, Wisconsin (GAL) [*Richardson et al.*, 2011]; (3) three towers within the Regional
280 Atmospheric Continuous CO₂ Network in the Rocky Mountains (RACCOON) [Stephens et al.,
281 2011], located in Storm Peak Lab, Colorado (SPL), Niwot Ridge, Colorado (NWR), and Hidden
282 Peak Snowbird, Utah (HDP); (4) seven towers supported by Environment Canada, located in
283 Fraserdale, Ontario (FRD), Egbert, Ontario (EGB), Candle Lake, Saskatchewan (CDL), East Trout
284 Lake, Saskatchewan (ETL), Sable Island, Nova Scotia (SBL), Lac LaBiche, Alberta (LLB), and
285 Chibougamau, Quebec (CHI); (5) five Oregon towers operated by Oregon State University

286 [Göckede *et al.*, 2010], including the Fir (FIR), Metolius (MET), Yaquina Head (YAH), Mary's
287 Peak (MAP), and Burns Old (NGB); and (6) four additional towers, located at the Harvard Forest,
288 Massachusetts (HFM) [Urbanski *et al.*, 2007], Morgan Monroe State Forest, Illinois (MMS)
289 [Dragoni *et al.*, 2007; Schmid *et al.*, 2000], Southern Great Plains, Oklahoma (SGP), and La Jolla,
290 CA (LJA) [Keeling *et al.*, 2005].

291 We use ~2,400 three-hour average CO₂ observations that have been filtered and processed as in
292 Fang and Michalak [2014] for use in inverse modeling applications by removing anomalous data
293 due to low-quality flags, extreme outliers, large deviations (+/- 30ppm) from the background,
294 possible transport-model concerns, and ocean sensitivity. Additionally, we remove the influence
295 of boundary conditions from the atmospheric measurements as in Fang *et al.* [2014]. The names,
296 locations, and measurement times of the CO₂ observations are given in Appendix 1.

297 In the synthetic data case study, the “ground-truth” for biospheric fluxes was obtained from the
298 Carnegie Ames Stanford Approach (CASA) model as configured for the Global Fire Emissions
299 Database (GFED) v2 project [Randerson *et al.*, 1997; van der Werf *et al.*, 2006]. These simulated
300 fluxes were obtained from model runs submitted to the North American Carbon Program Regional
301 Interim Synthesis [for details see Huntzinger *et al.*, 2012]. The estimates for FF fluxes were
302 obtained from the Vulcan (USA; 2002) and ODIAC (Canada, Mexico and Alaska; 2007)
303 inventories [Gurney *et al.*, 2009; Oda and Maksyutov, 2011]. These were then scaled to 2008 to
304 account for changes in the FF fluxes from those reported in these inventories. Since the CASA-
305 GFED v2 biospheric fluxes were available only at monthly scale they were downscaled to 3-hourly
306 temporal resolution by using net shortwave radiation and near-surface temperature data from the
307 NASA Global Land Data Assimilation System [Olsen and Randerson, 2004; GLDAS; Rodell *et*

308 *al.*, 2004]. Finally, synthetic observations were generated by adding (1) the estimates of FF fluxes
309 from Vulcan and ODIAC and, (2) biospheric fluxes from CASA-GFED v2 model at 3-hourly
310 resolution and transporting them forward (e.g., $[\mathbf{H}_{bio} \quad \mathbf{H}_{ff}](\mathbf{s}_{ff} + \mathbf{s}_{bio})$) through sensitivity
311 matrix $[\mathbf{H}_{bio} \quad \mathbf{H}_{ff}]$.

312 **3.2 Real Data Case Studies**

313 The real data case studies were designed to test the influence of a FF inventory in explaining
314 variations in inferred FF fluxes and disaggregating them from biospheric fluxes. This is achieved
315 by examining a posteriori cross-covariances and results of the model selection. Thus in one case
316 study, the model selection scheme (see section 2.4) is allowed to select covariates and an error
317 covariance model for FF fluxes from the full superset given in section 2.3 (henceforth, RD1),
318 whereas in the second case study this superset excludes covariate and error covariance model based
319 on FF inventory (henceforth, RD2). This distinction was made to explore the additional
320 error/uncertainty incurred due to the lack of a detailed inventory, a realistic constraint in many
321 parts of the world.

322 **3.3 Synthetic Data Case Study**

323 The goal of the synthetic data case study (henceforth, SD) was to evaluate the performance of the
324 inversion method when true fluxes are known. Its results provide a two-way indication of the
325 performance of the proposed method in disaggregating fluxes, that is (1) through analysis of a
326 posteriori cross-covariance between FF and biospheric fluxes, and (2) through comparison of the
327 estimated fluxes with true fluxes (see section 4). Overall, this case study is similar to the RD2, as
328 FF inventory estimates are not used as candidate covariates in \mathbf{X}_{ff} or \mathbf{Q}_{ff} . This is because in this

329 case the synthetic CO₂ observations are themselves generated using inventory datasets, and using
 330 this same dataset in the inversion would have provided an unrealistic amount of information about
 331 the true fluxes to the inversion. A zero-mean Gaussian white noise with variances equal to those
 332 in the model-data mismatch matrix (**R**) in RD2 was added to the synthetic CO₂ observations. **R** in
 333 SD is fixed to equal that in RD2, whereas the **Q_{ff}** and **Q_{bio}** covariance parameters and covariates
 334 are obtained from the procedure described in section 2.4. The quality of disaggregation is
 335 examined by comparing the inferred fluxes with the true fluxes i.e., CASA-GFED v2 biospheric
 336 and Vulcan and ODIAC FF fluxes.

337 **3.4 Framework for Evaluating Case Studies**

338 The Frobenius norm [for description see *Golub and Van Loan, 2012*] of FF and biospheric a
 339 posteriori cross-covariances is computed to check for the quality of the separation of the estimated
 340 fluxes. To compute the Frobenius norm of cross-covariances, the a posteriori covariances are first
 341 aggregated temporally to monthly resolution at grid scale to evaluate the degree to which
 342 biospheric and FF fluxes can be isolated at timescales relevant for understanding carbon budgets.
 343 This monthly covariance is obtained through the law of the sum of the variance of random variables
 344 in space and time and can be written as:

$$\bar{\mathbf{V}} = \begin{bmatrix} \bar{\mathbf{V}}_{bio} & \bar{\mathbf{V}}_{ff,bio}^T \\ \bar{\mathbf{V}}_{ff,bio} & \bar{\mathbf{V}}_{ff} \end{bmatrix} \quad (12)$$

345 where $\bar{\mathbf{V}}$ is a posteriori covariance of the fluxes aggregated to monthly temporal resolution, $\bar{\mathbf{V}}_{bio}$
 346 and $\bar{\mathbf{V}}_{ff}$ are a posteriori covariances of the biospheric and FF fluxes at monthly resolution,

347 respectively, and $\bar{\mathbf{V}}_{ff,bio}$ represents their cross-covariance. The Frobenius norm for $\bar{\mathbf{V}}_{ff,bio}$ is
 348 computed as:

$$\|\bar{\mathbf{V}}_{ff,bio}\|_F = \sqrt{\text{Trace}(\bar{\mathbf{V}}_{ff,bio}^T \bar{\mathbf{V}}_{ff,bio})} \quad (13)$$

349 where $\|\cdot\|$ stands for the norm, and all other terms are as defined earlier. A smaller Frobenius
 350 norm of $\bar{\mathbf{V}}_{ff,bio}$ indicates better separation of the two signals and low a posteriori cross-covariance
 351 between the disaggregated fluxes.

352 The model resolution matrix of the estimated FF fluxes at the 8-day temporal resolution was also
 353 examined. The model resolution matrix indicates the quality of estimated fluxes, and can be given
 354 as:

$$\hat{\mathbf{m}}_{ff} = \mathbf{\Lambda}_{ff}^T \mathbf{H}_{ff} \quad (12)$$

355 where $\hat{\mathbf{m}}_{ff}$ is the model resolution matrix and all other terms are as described earlier. The quality
 356 of the estimated FF fluxes is assessed by computing the ℓ^2 norm of $\hat{\mathbf{m}}_{ff}$. A ℓ^2 norm of 1 of $\hat{\mathbf{m}}_{ff}$
 357 indicates that estimated FF fluxes can be independently determined, whereas a value greater than
 358 1 indicates that only average fluxes can be determined, with progressively larger ℓ^2 norms
 359 indicating progressively poor estimation of FF fluxes [for details see: *Menke 2012*].

360 The correlation between true and modeled concentration was also examined for the two real data
 361 case studies.

362 **4 Results and Discussion**

363 The quantification of fossil fuel emissions from atmospheric observations depends the availability
 364 of an observational network that is sufficiently sensitive to FF emissions and the methodological

365 framework for isolating the biospheric and FF components of the terrestrial fluxes. An approach
366 for fulfilling the second of these needs is presented here. This approach is evaluated within four
367 regions of the United States (Figure 1), because these are the regions for which the observational
368 network in 2008 was relatively more effective at detecting FF emissions [Shiga *et al.*, 2014].

369 For the RD1 case study, the fossil fuel inventory is selected both as the spatial trend of the FF
370 emissions (\mathbf{X}_{ff}), and as the dataset used to populate the error covariance matrix (\mathbf{Q}_{ff}). Intuitively,
371 in the context of the inversion case studies, the choice of a FF trend and error covariance model
372 selected by BIC implies that among all candidate models it is best suited for: (1) describing the
373 variance in the spatial distribution of FF emissions, (2) identifying the FF signal in the CO₂
374 observations, (3) separating FF and biospheric fluxes, and (4) computing estimates of FF and
375 biospheric fluxes. The selection of the FF inventory by BIC in the RD1 case is not a surprise, as
376 this inventory is indeed expected to be more representative of the true FF emissions patterns
377 relative to the other candidate variables. Moreover, it also shows that covariates of FF emissions
378 with high spatio-temporal resolution (e.g., diurnally and seasonally varying) are more
379 representative of the true distribution of FF fluxes relative to covariates that do not vary in time
380 (e.g., urban areas). Covariates of FF fluxes that typically vary at daily temporal resolution were
381 included in this study but they did not have any temporal variability as we did not have access to
382 these data (e.g., Landsat population density data) or due to non-availability of data at this
383 temporal resolution (e.g., night lights).

384 Results from RD1 confirm that the statistical framework presented here can be used to
385 disaggregate biospheric and FF terrestrial CO₂ fluxes when observations are sufficiently sensitive
386 to FF emissions. The success of the disaggregation of FF and biospheric fluxes in RD1 can be

387 evaluated by examining the a posteriori cross-covariance and cross-correlation of uncertainties
388 (Figure 2; also see Appendix 2) between these component flux estimates at aggregated spatial (i.e.
389 regional) and temporal (i.e. monthly) scales. The cross-covariances are generally small relative to
390 the magnitude of the fluxes (Figure 2), and the cross-correlations are low, except for the Midwest.
391 An inversion was also performed for July (results not shown) for all three case studies. This was
392 done to test our ability to disaggregate FF fluxes from biospheric fluxes in a summer month. We
393 found that both ℓ^2 and Frobenius norm for January (eq. 13, Table 1) was over a factor of 15 times
394 lower than those obtained for July and fossil fuel emissions were not detectable by the
395 measurement network due to the large confounding influence of the biospheric fluxes (see also
396 Shiga et al. 2014). The small Frobenius norm in January is another indication of the small cross-
397 covariances between the FF and biospheric flux uncertainties. This is further confirmed by the ℓ^2
398 norm of the model resolution matrix (see eq. 14, and Table 1) and the coefficient of determination
399 of 0.84 (see, Appendix 4) between the true and posteriori fit of observations obtained by
400 transporting forward the estimated fluxes for the month of January 2008.

401 For the RD2 case study, the fossil fuel inventory is made unavailable for the variable selection (for
402 both the trend (\mathbf{X}_{ff}) and prior error covariance (\mathbf{Q}_{ff}) models). This leads to the selection of mean
403 population density, percent urban land cover (\mathbf{X}_{ff}) and the maximum value of night lights intensity
404 (\mathbf{Q}_{ff}) as alternatives (Table 1). The impact of using these datasets, which are less directly
405 representative of the underlying FF emissions, is seen via increased cross-covariances (Figure 2)
406 and cross-correlations in the monthly regional posterior uncertainties of the biospheric and FF
407 fluxes in the RD2 case study. The Frobenius norm, ℓ^2 norm (Table 1), and correlation between true
408 and posterior fit of observations (Appendix 4) as in RD1 is low and the estimates of total fluxes

409 (Figure 3) show similar uncertainties on the total flux relative to RD1 (Figure 3), but increased
410 uncertainties on the component contributions from FF and biospheric fluxes.

411 For the SD case study, the fossil fuel inventory is also made unavailable for the variable selection,
412 as it is used to create the synthetic observations. The selected alternate covariates are night light
413 intensity and population density (\mathbf{X}_{ff}) and the variance of population density within each 1° by 1°
414 gridcells (\mathbf{Q}_{ff}) (Table 1). These are different from the ones selected in RD2. This is due to the
415 differences between the RD and SD setups, including the nature of the true FF fluxes and the
416 impact of transport model errors. The effect of using these datasets, which are proxies of FF
417 emissions, on the posterior cross-covariances and cross-correlations (Figure 2) in the biospheric
418 and FF uncertainties is similar to that observed in RD2, though with a lower Frobenius norm of
419 $\bar{\mathbf{V}}_{ff,bio}$ relative to RD2 case study.

420 For the SD case study, the FF, biospheric, and total fluxes can also be compared to their “true”
421 values (Figure 4). Results confirm that, although the separation of FF and biospheric flux become
422 more uncertain in the absence of a good inventory, the separation is still relatively robust, in the
423 sense that the true fluxes lie within the range of the posterior uncertainties. The poorest
424 performance is in the Midwest, which is also the region with the highest cross-covariance and
425 cross-correlation in the posterior uncertainties. Another indication of the good overall
426 performance of the flux disaggregation is the low RMSE of the 1° by 1° fluxes at the native
427 temporal resolution of the inversion (3-hourly for biospheric fluxes, 8-day for FF fluxes), namely
428 $0.33 \mu\text{mol m}^2\text{sec}^{-1}$ for FF emissions and $0.22 \mu\text{mol m}^2 \text{sec}^{-1}$ for biospheric fluxes, relative to the
429 magnitude of the fluxes (Figure 4).

430

431 **5 Conclusions**

432 With increasing attention being placed on accurate monitoring of FF emissions, the ability to
433 provide a top-down verification of inventory-based estimates of FF emissions, by disaggregating
434 FF and biospheric fluxes, is a promising development. The sparsity of in-situ measurement
435 networks, the small relative contribution of FF flux to the total observed CO₂ fluctuations,
436 especially during the growing season and the large model-data mismatch errors due, in large part,
437 to uncertainties associated with modeling of atmospheric transport severely limit the ability of
438 inverse models to accurately estimate FF emissions.

439 Assuming that there is low systematic bias in WRF-STILT transport model, the analyses described
440 in this paper demonstrate, that the proposed method is successful in separating FF and biospheric
441 fluxes at sub-continental scales. This confirms the potential of using a statistical approach, based
442 on the unique spatiotemporal signature of FF emissions, to isolate and estimate FF emissions using
443 CO₂ observations.

444 Our method performs the disaggregation of biospheric and FF CO₂ emissions using error
445 covariance models and flux covariates (e.g. night lights, population density among others) that are
446 specific to biospheric and FF fluxes. These models and covariates are quite different for the two
447 flux components and are fundamental to a successful disaggregation. We find that using a FF
448 inventory to construct an error covariance model for FF fluxes provides a better disaggregation
449 relative to the case when static proxies of FF fluxes are used. This is due to the better
450 spatiotemporal fidelity that an inventory provides to the FF fluxes being estimated, relative to the
451 other proxies. The synthetic data case study shows that even in the absence of a detailed FF

452 inventory, other static FF related variables can provide sufficient information to adequately
453 disaggregate and estimate FF and biospheric fluxes.

454 In both cases, the ability to disaggregate flux components is predicated on the availability of a
455 monitoring network that is sufficiently sensitive to both types of fluxes. The addition of column-
456 averaged dry air mole fraction observations [*Kuai et al. 2013*] from satellites [for list of satellites
457 that measure CO₂ see *Kulawik et al. 2013*] and tracers that provide independent information on FF
458 emissions would undoubtedly further improve the FF emission estimates.

459 The ability to accurately disaggregate and estimate FF and biospheric fluxes using atmospheric
460 data is a continuing challenge. This pursuit relies heavily on external conditions including, but not
461 limited, to the representativeness and density of the observational network as well as transport
462 model accuracy. Nevertheless, the methodological advances presented here, specifically the
463 exploitation of the unique spatiotemporal structure of FF emissions, offers an approach to
464 optimally leverage the information content of available data to provide a complementary approach
465 for estimating FF fluxes.

466

467

468

469

470 **Acknowledgements**

471 This work was supported by Sandia National Laboratories' LDRD (Laboratory Directed Research
472 and Development) funds, sponsored by the Geosciences Investment Area. Sandia National

473 Laboratories is a multi-program laboratory managed and operated by Sandia Corporation, a wholly
474 owned subsidiary of Lockheed Martin Corporation, for the US Department of Energy's National
475 Nuclear Security Administration under contract DE-AC04-94AL85000.

476 We gratefully acknowledge the efforts of the PIs of the various towers providing continuous
477 atmospheric CO₂ observations, which were instrumental for this analyses. The sites BRW, WGC,
478 SNP, SCT, AMT, WBI, BAO, LEF and WKT are part of NOAA's Global Greenhouse Gas
479 Reference Network operated by the Global Monitoring Division of NOAA's Earth System
480 Research Laboratory with additional support from NOAA's Climate Program Office and are a
481 contribution to the North American Carbon Program. The installation of CO₂ sampling equipment
482 was made possible at AMT, by a grant from the National Science Foundation Biocomplexity in
483 the Environment Program (ATM-0221850), at SNP, by the University of Virginia, and at SCT by
484 funding provided by the DOE Office of Science – Terrestrial Carbon Processes program. The
485 Savannah River National Laboratory (SRNL) provided support during the installation at SCT and
486 provides ongoing support via funding from NOAA. SNRL is operated by Savannah River Nuclear
487 Solutions, LLC under Contract No. DE-AC09-08SR22470 with the US Department of Energy.
488 WGC measurements were supported by a combination of the California Energy Commission's
489 Public Interest Environmental Research Program to the Lawrence Berkeley National Laboratory
490 under contract DE-AC02-05CH11231 and NOAA. Research at CVA, OZA, KEW, CEN, MEA,
491 ROL and GAL was sponsored by the U.S. Department of Energy Office of Science TCP program
492 (DE-FG02-06ER64315) and by the U.S. Department of Commerce, NOAA office of Global
493 Programs (NA08OAR4310533). The five Oregon sites FIR, MET, YAH, MAP, NGB were
494 supported by NOAA (NA11OAR4310056). The research at the MMS site was sponsored by the

495 U.S. Department of Energy through the Ameriflux Management Project, the Midwestern Center
496 of the National Institute for Global Environmental Change (NIGEC), the National Institute for
497 Climate Change Research (NICCR), the Terrestrial Carbon Program (TCP), and the Terrestrial
498 Ecosystem Sciences (TES) programs. CO₂ measurements at LJA were supported by the Scripps
499 CO₂ program.

500 We thank the following individuals for collecting and providing the atmospheric CO₂ data from
501 the following sites: Arlyn Andrews (NOAA) for SNP, AMT, WBI, BAO, LEF and WKT, Kirk
502 Thoning (NOAA) for BRW, Matthew J. Parker (SRNL) for SCT, Marc Fischer (LBNL) and Arlyn
503 Andrews (NOAA) for WGC, Kenneth Davis, Scott Richardson and Natasha Miles (The
504 Pennsylvania State University) for CVA, OZA, KEW, CEN, MEA, ROL and GAL, Britton
505 Stephens (NCAR) and the Regional Atmospheric Continuous CO₂ Network in the Rocky
506 Mountains (RACCOON) for NWR, SPL and HDP, Beverly Law (Oregon State University) and
507 the TERRA-PNW group for data from 5 Oregon sites, FIR, MET, YAH, MAP, and NGB, William
508 Munger (Harvard University) and Steven Wofsy (Harvard University) for HFM, Doug Worthy
509 (Environment Canada) for CDL, FRD, SBL, EGB, ETL, LLB, and CHM, Kimberly Novick
510 (Indiana University) for MMS, Sebastien Biraud (LBNL) and Margaret Torn (LBNL) for SGP and
511 Ralph Keeling (Scripps Institution of Oceanography) and Lisa Welp (Purdue University) for LJA.

512 Note: All the code required for evaluating, replicating and building upon the results of this paper
513 can be obtained without cost from Vineet Yadav by contacting him through email at
514 vineet.yadav@jpl.nasa.gov. For obtaining the concentration data utilized in this study, researchers
515 would have to directly (on their own) contact the principal investigators of towers listed above.

516 **Figures, Table and Appendix Captions**

517 Table 1: Covariates and error covariance models selected by BIC for \mathbf{X}_{ff} and \mathbf{Q}_{ff} for the three
 518 case studies

519

Case Studies	Covariates					FF Covariance Model	Frobenius Norm ($\mu\text{mol m}^{-2}\text{sec}^{-1}$) ²	ℓ^2 norm of model resolution matrix
	Mean Night Light Intensity	Mean Population Density	% Built Up Area	% Urban Area	FF Inventory			
RD1					✓	Mean (FF Inventory)	6.92	2.53
RD2		✓		✓	N/A	Maximum (Night Lights Intensity)	9.69	4.86
SD	✓	✓			N/A	Variance (Population Density; per sq. km)	6.95	3.53

520

521

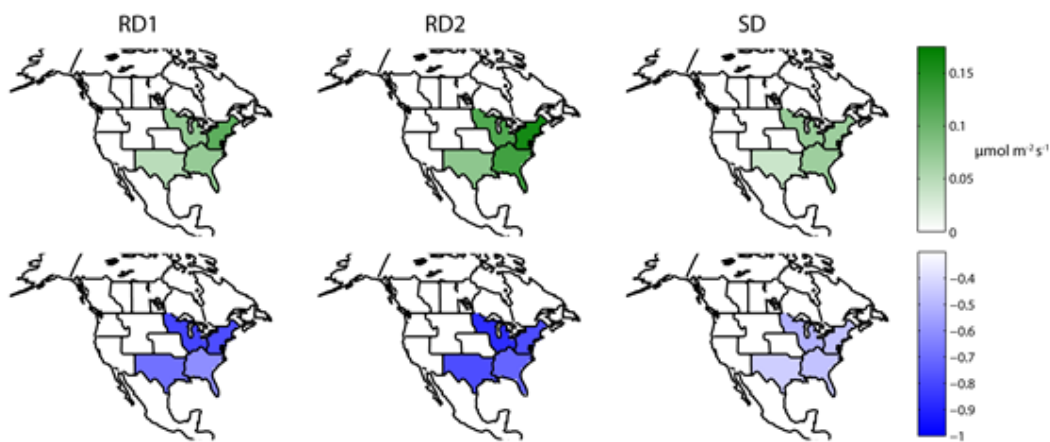
522 Figure 1: Regional classification map for aggregating fluxes and a posteriori cross-covariances of
523 biospheric and fossil fuel fluxes.

524



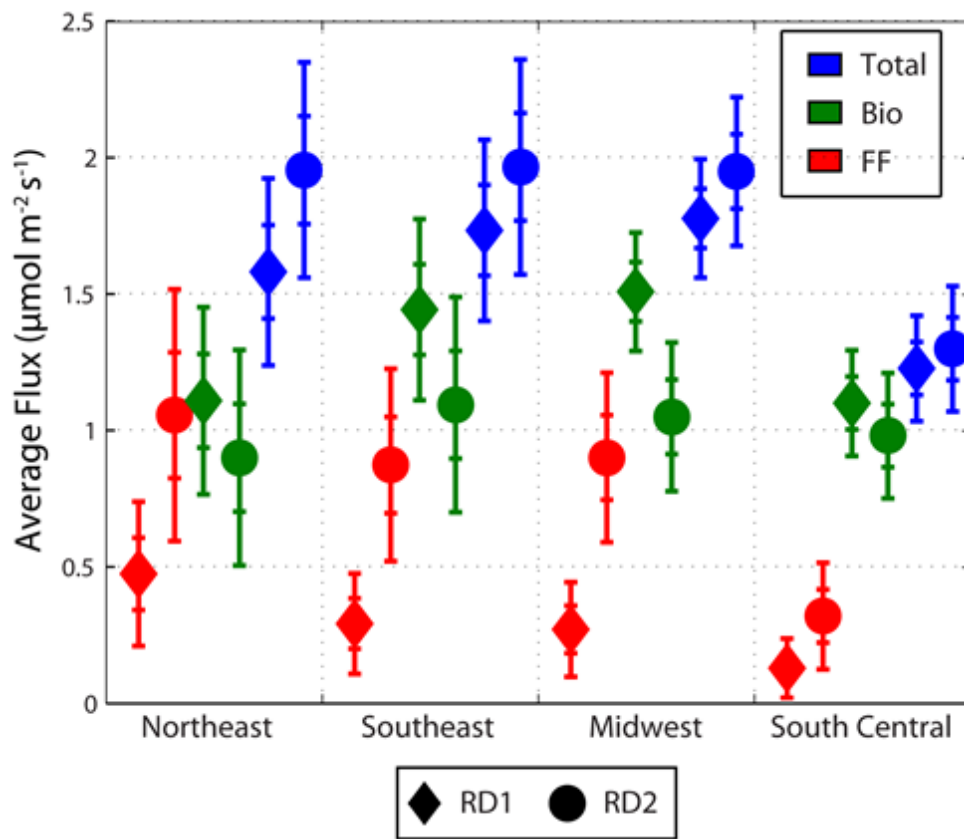
525

526 Figure 2: Row 1 represents the a posteriori cross-covariances* of the FF and biospheric fluxes,
527 aggregated a posteriori to monthly temporal resolution and regional spatial scale for the three case
528 studies. Row 2 shows the correlation coefficients of these a posteriori uncertainties. Smaller
529 covariances and correlation coefficients imply better separation between fossil fuel and biospheric
530 flux estimates.



531
532 *Note: Shown here is square root of the absolute value of the cross-covariance ($\bar{V}_{ff,bio}$) to be
533 comparable to uncertainty bounds from Figures 3 and 4.
534

535 Figure 3: Estimates of the fossil fuel, biospheric, and total flux with one standard deviation (first
536 hash mark) and two standard deviation uncertainty bounds for the regions shown in Figure 1 for
537 the two real data case studies. Diamonds represent RD1; circles represent RD2.

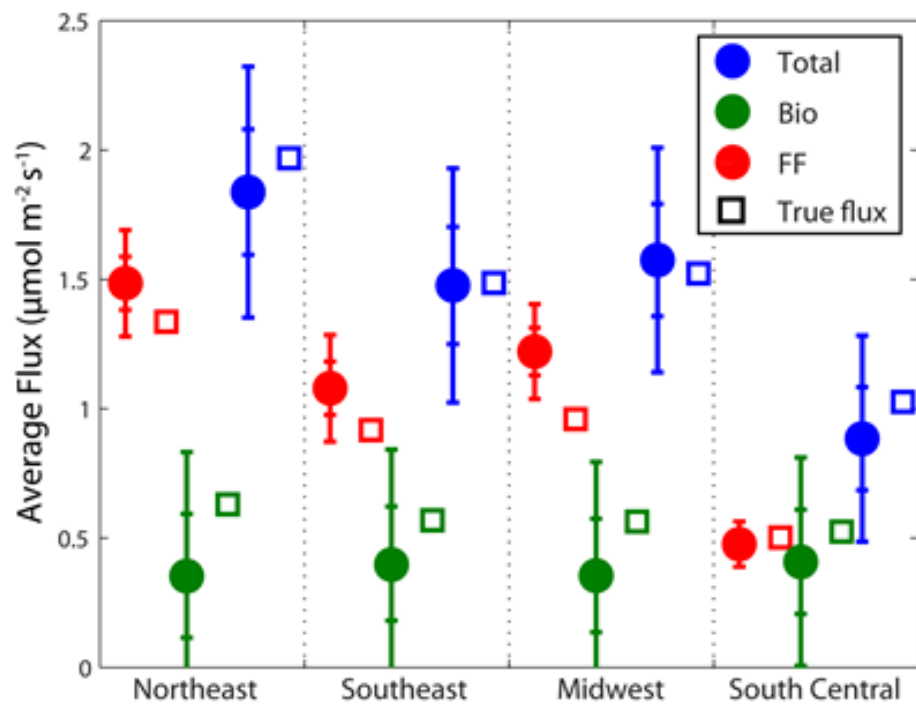


538

539

540

541 Figure 4: Estimates of fossil fuel, biospheric and total fluxes with one standard deviation (first
542 hash mark) and two standard deviation uncertainty bounds for the regions shown in Figure 1 for
543 the synthetic data case.



544

545

546 **References**

- 547 Brioude, J., et al. (2012), A new inversion method to calculate emission inventories without a prior
548 at mesoscale: Application to the anthropogenic CO₂ emission from Houston, Texas, *Journal of*
549 *Geophysical Research-Atmospheres*, 117, D05312, doi: 10.1029/2011jd016918
- 550 Cambaliza, M., P. Shepson, D. Caulton, B. Stirm, D. Samarov, K. Gurney, J. Turnbull, K. Davis,
551 A. Possolo, and A. Karion (2013), Assessment of uncertainties of an aircraft-based mass-balance
552 approach for quantifying urban greenhouse gas emissions, *Atmospheric Chemistry & Physics*
553 *Discussions*, 13, 29895-29945
- 554 CIESIN (2012), Center for International Earth Science Information Network (CIESIN), Columbia
555 University. National Aggregates of Geospatial Data: Population, Landscape and Climate Estimates
556 Version 3 (PLACE III), Palisades, NY: CIESIN, Columbia University. Available at:
557 <http://sedac.ciesin.columbia.edu/data/set/nagdc-population-landscape-climate-estimates-v3>.
- 558 Christen, A. (2014), Atmospheric measurement techniques to quantify greenhouse gas emissions
559 from cities, *Urban Climate*, 10, 241-260.
- 560 Cressie, N. A. C. (1993), *Statistics for spatial data*, 928pp., Wiley. New York.
- 561 Crisp, D., et al. (2004), The orbiting carbon observatory (OCO) mission, *Trace Constituents in the*
562 *Troposphere and Lower Stratosphere*, 34(4), 700-709.
- 563 Duren, R. M., and C. E. Miller (2012), Measuring the carbon emissions of megacities, *Nature*
564 *Climate Change*, 2(8), 560-562.

565 Elvidge, C. D., K. E. Baugh, E. A. Kihn, H. W. Kroehl, and E. R. Davis (1997), Mapping city
566 lights with nighttime data from the DMSP Operational Linescan System, *Photogrammetric*
567 *Engineering and Remote Sensing*, 63(6), 727-734.

568 Fang, Y., A. Michalak, Y. Shiga, and V. Yadav (2014), Using atmospheric observations to evaluate
569 the spatiotemporal variability of CO₂ fluxes simulated by terrestrial biospheric models,
570 *Biogeosciences Discussions*, 11(6), 9215-9247.

571 George, K., L. H. Ziska, J. A. Bunce, and B. Quebedeaux (2007), Elevated atmospheric CO₂
572 concentration and temperature across an urban–rural transect, *Atmospheric Environment*, 41(35),
573 7654-7665.

574 Göckede, M., A. M. Michalak, D. Vickers, D. P. Turner, and B. E. Law (2010), Atmospheric
575 inverse modeling to constrain regional scale CO₂ budgets at high spatial and temporal resolution,
576 *J. Geophys. Res.*, 115(D15), D15113.

577 Golub, G. H., and C. F. Van Loan (2012), *Matrix computations*, 784pp., The John Hopkins
578 University Press. Baltimore. Maryland

579 Gourdji, S., A. Hirsch, K. Mueller, V. Yadav, A. Andrews, and A. Michalak (2010), Regional-
580 scale geostatistical inverse modeling of North American CO₂ fluxes: a synthetic data study,
581 *Atmos. Chem. Phys.*, 10, 6151-6167.

582 Gourdji, S. M., K. L. Mueller, V. Yadav, D. N. Huntzinger, A. E. Andrews, M. Trudeau, G. Petron,
583 T. Nehrkorn, J. Eluszkiewicz, and J. Henderson (2012a), North American CO₂ exchange: inter-
584 comparison of modeled estimates with results from a fine-scale atmospheric inversion,
585 *Biogeosciences*, 9, 457-475.

586 Gourджи, S. M., et al. (2012b), North American CO₂ exchange: inter-comparison of modeled
587 estimates with results from a fine-scale atmospheric inversion, *Biogeosciences*, 9(1), 457-475.

588 Gratani, L., and L. Varone (2005), Daily and seasonal variation of CO₂ in the city of Rome in
589 relationship with the traffic volume, *Atmospheric Environment*, 39(14), 2619-2624.

590 Gurney, K. R., I. Razlivanov, Y. Song, Y. Zhou, B. Benes, and M. Abdul-Massih (2012),
591 Quantification of Fossil Fuel CO₂ Emissions on the Building/Street Scale for a Large U.S. City,
592 *Environ. Sci. Technol.*, 46(21), 12194-12202.

593 Gurney, K. R., D. L. Mendoza, Y. Zhou, M. L. Fischer, C. C. Miller, S. Geethakumar, and S. de
594 la Rue du Can (2009), High Resolution Fossil Fuel Combustion CO₂ Emission Fluxes for the
595 United States, *Environ. Sci. Technol.*, 43(14), 5535-5541.

596 Gurney, K. R., et al. (2002), Towards robust regional estimates of CO₂ sources and sinks using
597 atmospheric transport models, *Nature*, 415, 626-630.

598 Huntzinger, D., W. M. Post, Y. Wei, A. Michalak, T. O. West, A. Jacobson, I. Baker, J. M. Chen,
599 K. Davis, and D. Hayes (2012), North American Carbon Program (NACP) regional interim
600 synthesis: Terrestrial biospheric model intercomparison, *Ecological Modelling*, 232, 144-157.

601 Idso, C. D., S. B. Idso, and R. C. Balling (2001), An intensive two-week study of an urban CO₂
602 dome in Phoenix, Arizona, USA, *Atmospheric Environment*, 35(6), 995-1000.

603 Kitanidis, P. K. (1995), Quasi-Linear Geostatistical Theory for Inversing, *Water Resources*
604 *Research*, 31(10), P.-2411.

605 Kort, E. A., C. Frankenberg, C. E. Miller, and T. Oda (2012), Space-based observations of
606 megacity carbon dioxide, *Geophysical Research Letters*, 39., L17806,
607 doi:10.1029/2012GL052738.

608 Lauvaux, T., N. L. Miles, S. J. Richardson, A. Deng, D. R. Stauffer, K. J. Davis, G. Jacobson, C.
609 Rella, G.-P. Calonder, and P. L. DeCola (2013), Urban emissions of CO₂ from Davos,
610 Switzerland: the first real-time monitoring system using an atmospheric inversion technique,
611 *Journal of Applied Meteorology and Climatology*, 52(12), 2654-2668.

612 Lin, J. C., C. Gerbig, S. C. Wofsy, A. E. Andrews, B. C. Daube, K. J. Davis, and C. A. Grainger
613 (2003), A near-field tool for simulating the upstream influence of atmospheric observations: The
614 Stochastic Time-Inverted Lagrangian Transport (STILT) model, *Journal of Geophysical Research:*
615 *Atmospheres*, vol. 108, NO. D16, 4493, doi:10.1029/2002JD003161.

616 Matese, A., B. Gioli, F. Vaccari, A. Zaldei, and F. Miglietta (2009), Carbon dioxide emissions of
617 the city center of Firenze, Italy: measurement, evaluation, and source partitioning, *Journal of*
618 *Applied Meteorology and Climatology*, 48(9), 1940-1947.

619 Mays, K. L., P. B. Shepson, B. H. Stirm, A. Karion, C. Sweeney, and K. R. Gurney (2009),
620 Aircraft-based measurements of the carbon footprint of Indianapolis, *Environ. Sci. Technol.*,
621 43(20), 7816-7823.

622 McKain, K., Wofsy, S., Nehrkorn, T., Eluszkiewicz, J., Ehrlinger, J. R., and Stephens, B. B.:
623 Assessment of ground-based atmospheric observations for verification of greenhouse gas
624 emissions from an urban region, *P. Natl. Acad. Sci. USA*, 109, 8423-8428, 2012.

625

626 Michalak, A. M., and P. K. Kitanidis (2003), A method for enforcing parameter nonnegativity in
627 Bayesian inverse problems with an application to contaminant source identification, *Water*
628 *Resources Research*, 39, 2, 1033, 10.1029/2002WR001480.

629 Michalak, A. M., L. Bruhwiler, and P. P. Tans (2004), A geostatistical approach to surface flux
630 estimation of atmospheric trace gases, *Journal of Geophysical Research*, 109, D14109.

631 Miller, J. B., et al. (2012), Linking emissions of fossil fuel CO₂ and other anthropogenic trace
632 gases using atmospheric ¹⁴CO₂, *Journal of Geophysical Research*, 117, 23-PP.

633 Miller, S. M., A. M. Michalak, and P. J. Levi (2014), Atmospheric inverse modeling with known
634 physical bounds: an example from trace gas emissions, *Geoscientific Model Development*, 7(1),
635 303-315.

636 Miteva, B. (2002), *Atlas of the Biosphere: Built-Up Land*, edited by N. I. f. E. Studies, University
637 of Wisconsin - Madison, Madison, WI.

638 Newman, S., X. Xu, H. P. Affek, E. Stolper, and S. Epstein (2008), Changes in mixing ratio and
639 isotopic composition of CO₂ in urban air from the Los Angeles basin, California, between 1972
640 and 2003, *Journal of Geophysical Research: Atmospheres* (1984–2012), 113(D23).

641 Oda, T., and S. Maksyutov (2011), A very high-resolution (1 km x 1 km) global fossil fuel CO₂
642 emission inventory derived using a point source database and satellite observations of nighttime
643 lights, *Atmospheric Chemistry and Physics*, 11(2), 543-556.

644 Olsen, S. C., and J. T. Randerson (2004), Differences between surface and column atmospheric
645 CO₂ and implications for carbon cycle research, *Journal of Geophysical Research: Atmospheres*,
646 vol. 109, D02301, doi:10.1029/2003JD003968.

647 Pacala, S., et al. (2010), Verifying Greenhouse Gas Emissions: Methods to Support International
648 Climate Agreements. Committee on Methods for Estimating Greenhouse Gas Emissions, National
649 Research Council Report, 124 pp., The National Academies Press, Washington, D.C.

650 Randerson, J. T., M. V. Thompson, T. J. Conway, I. Y. Fung, and C. B. Field (1997), The
651 contribution of terrestrial sources and sinks to trends in the seasonal cycle of atmospheric carbon
652 dioxide, *Global Biogeochemical Cycles*, vol 11, NO. 4, pp 535-560.

653 Ray, J., V. Yadav, A. M. Michalak, B. van Bloemen Waanders, and S. A. Mckenna. (2014), A
654 multiresolution spatial parameterization for the estimation of fossil-fuel carbon dioxide emissions
655 via atmospheric inversions. *Geoscientific Model Development* 7(5), 1901-1918,
656 doi: 10.5194/gmdd-7-1277-2014

657 Ray, J., J. Lee, V. Yadav, S. Lefantzi, A. M. Michalak, and B. van Bloemen Waanders. (2014), A
658 sparse reconstruction method for the estimation of multiresolution emission fields via atmospheric
659 inversion. *Geoscientific Model Development Discussions*, 7(4), 5623-5659, doi:10.5194/gmdd-7-
660 5623-2014

661 Rayner, P. J., I. G. Enting, R. J. Francey, and R. Langenfelds (1999), Reconstructing the recent
662 carbon cycle from atmospheric CO₂, delta13C and O₂/N₂ observations, *Tellus B*, 51(2), 213-232.

663 Reid, K., and D. Steyn (1997), Diurnal variations of boundary-layer carbon dioxide in a coastal
664 city-Observations and comparison with model results, *Atmospheric Environment*, 31(18), 3101-
665 3114.

666 Rice, A., and G. Bostrom (2011), Measurements of carbon dioxide in an Oregon metropolitan
667 region, *Atmospheric Environment*, 45(5), 1138-1144.

668 Rigby, M., R. Toumi, R. Fisher, D. Lowry, and E. G. Nisbet (2008), First continuous
669 measurements of CO₂ mixing ratio in central London using a compact diffusion probe,
670 *Atmospheric Environment*, 42(39), 8943-8953.

671 Rodell, M., P. Houser, U. e. a. Jambor, J. Gottschalck, K. Mitchell, C.-J. Meng, K. Arsenault, B.
672 Cosgrove, J. Radakovich, and M. Bosilovich (2004), The global land data assimilation system,
673 *Bulletin of the American Meteorological Society*, vol 85, NO. 3, pp 381-394, doi 10.1175/BAMS-
674 85-3-381

675 Schneider, A., M. A. Friedl, and D. Potere (2009), A new map of global urban extent from MODIS
676 satellite data, *Environ. Res. Lett.*, 4(4), 044003.

677 Schwarz, G. (1978), Estimating the Dimension of a Model, *The Annals of Statistics*, 6(2), 461-
678 464.

679 Shiga, Y. P., A. M. Michalak, S. M. Gourdjji, K. L. Mueller, and V. Yadav (2014), Detecting fossil
680 fuel emissions patterns from sub-continental regions using North American in-situ CO₂
681 measurements, *Geophysical Research Letters*, 41, pp 4381-4388, doi:10.1002/2014GL059684.

682 Sloop, C., and E. Novakovskaia (2012), Data from the Dense Atmospheric Observing Network to
683 Detect GHG Trends and Anomalies, paper presented at WMO Technical Conference on
684 Meteorological and Environmental Instruments and Methods of Observation, TECO-2012.

685 Snodgrass, M. F., and P. K. Kitanidis (1997), A geostatistical approach to contaminant source
686 identification, *Water Resour. Res.*, 33(4), 537- 546, 1997.

687 Stein, M. L. (1988), Asymptotically efficient prediction of a random field with a misspecified
688 covariance function, *The Annals of Statistics*, 16(1), 55-63.

689 Strong, C., C. Stwertka, D. Bowling, B. Stephens, and J. Ehleringer (2011), Urban carbon dioxide
690 cycles within the Salt Lake Valley: A multiple-box model validated by observations, *Journal of*
691 *Geophysical Research: Atmospheres* (1984–2012), 116(D15), doi: 10.1029/2011JD015693.

692 Tans, P. P., I. Y. Fung, and T. Takahashi (1990), Observational Constrains on the Global
693 Atmospheric Co₂ Budget, *Science*, 247(4949), 1431-1438.

694 van der Werf, G. R., J. T. Randerson, L. Giglio, G. J. Collatz, P. S. Kasibhatla, and J. A. F. Arellano
695 (2006), Interannual variability in global biomass burning emissions from 1997 to 2004,
696 *Atmospheric Chemistry and Physics*, 6, 3423-3441.

697 Velazco, V. A., M. Buchwitz, H. Bovensmann, M. Reuter, O. Schneising, J. Heymann, T. Krings,
698 K. Gerilowski, and J. P. Burrows (2011), Towards space based verification of CO₂ emissions from
699 strong localized sources: fossil fuel power plant emissions as seen by a CarbonSat constellation,
700 *Atmos. Meas. Tech.*, 4(12), 2809-2822.

701 Vogel, F. R., B. Tiruchittampalam, J. Theloke, R. Kretschmer, C. Gerbig, S. Hammer, and I. Levin
702 (2013), Can we evaluate a fine-grained emission model using high-resolution atmospheric
703 transport modelling and regional fossil fuel CO₂ observations?, *Tellus B*, 65.

704 Yadav, V., and A. M. Michalak (2013), Improving computational efficiency in large linear inverse
705 problems: an example from carbon dioxide flux estimation, *Geosci. Model Dev.*, 6, 583–590, doi:
706 10.5194, edited, gmd-6-583-2013.

707 Yadav, V., K. L. Mueller, and A. M. Michalak (2013), A backward elimination discrete
708 optimization algorithm for model selection in spatio-temporal regression models, *Environmental*
709 *Modelling & Software*, 42, 88-98.

710 Yadav, V., K. L. Mueller, D. Dragoni, and A. M. Michalak (2010), A geostatistical synthesis study
711 of factors affecting gross primary productivity in various ecosystems of North America,
712 *Biogeosciences*, 7(9), 2655-2671.

713 Zimnoch, M., J. Godlowska, J. Necki, and K. Rozanski (2010), Assessing surface fluxes of CO₂
714 and CH₄ in urban environment: a reconnaissance study in Krakow, Southern Poland, *Tellus B*,
715 62(5), 573-580.

716

717

718

719

720

721

722

723

724

725

726

727 Appendix 1: Locations and measurement times of CO₂ concentrations across study sites (in-situ
728 towers). Modified (removed sites with no data in January 2008) from: Shiga, Y. P., A. M.
729 Michalak, S. M. Gourdj, K. L. Mueller, and V. Yadav (2014), Detecting fossil fuel emissions

730 patterns from sub-continental regions using North American in-situ CO₂ measurements,
 731 Geophysical. Research. Letters, 41, 4381–4388, doi:10.1002/2014GL059684 (See Table S1 in the
 732 manuscript). Note that the variances or model-data mismatch (σ_R) are obtained a priori through Restricted
 733 Maximum Likelihood, from the method described in section 2.4

734

735

Tower	Name	Latitude	Longitude	Time of Day (Local Time, hours)	Height [m]	σ_R RD1 [ppm]	σ_R RD2 [ppm]
LEF	Park Falls	45.95	-90.27	1 4 7 10 13 16 19 22	396	1.49	1.41
WKT	Moody	31.32	-97.33	1 4 7 13 16 19 22	457	1.18	1.16
WBI	West Branch	41.73	-91.35	1 4 7 10 13 16 19 22	379	1.16	1.13
BAO	Boulder Observatory	40.05	-105.01	1 4 7 13 16 19 22	300	1.59	1.59
WGC	Walnut Grove	38.27	-121.49	1 4 7 13 16 19 22	483	5.39	5.34
AMT	Argyle	45.03	-68.68	13 16 19	107	2.99	2.84
BRW	Barrow	71.32	-156.61	1 4 7 10 13 16 19 22	17	0.01	0.09

FRD	Fraserdale	49.88	-81.57	13 16 19	40	2.64	0.56
CDL	Candle Lake	53.99	-105.12	13 16 19	30	1.56	0.58
SBL	Sable Island	43.93	-60.02	1 4 7 10 13 16 19 22	25	1.36	1.36
EGB	Egbert	44.23	-79.78	13	3	3.99	4.03
ETL	East Trout Lake	54.35	-104.99	10 13 16 19	105	3.35	0.86
LLB	Lac LaBiche	54.95	-112.45	13	10	3.03	2.99
CHI	Chibougamau	49.69	-74.34	13 16 19	30	0.48	0.47
HFM	Harvard Forest	42.54	-72.17	13 16 19	30	3.13	3.20
ARM	Southern Great Plains	36.8	-97.5	13 16 19	60	1.26	1.23
MOM	Morgan Monroe	39.32	-86.41	13 16 19	48	4.64	4.79
OZA	Ozark	38.74	-92.2	13 16 19	30	0.97	0.95
KEW	Kewanee	41.28	-89.97	13 16 19	140	1.95	1.88
CEN	Centerville	40.79	-92.88	13 16 19	110	0.90	0.91
MEA	Mead	41.14	-96.46	13 16 19	122	0.63	0.48
ROL	Round Lake	43.53	-95.41	13 16 19	110	1.14	1.04
GAL	Galesville	44.09	-91.34	13 16 19	122	2.02	2.03
NWR	Niwot Ridge	40.05	-105.58	1	5	2.2	1.21
HDP	Hidden Peak Snowbird	40.56	-111.65	1	18	0.82	0.81
FIR	Fir	44.65	-123.55	13 16 19	38	3.26	3.22

MET	Metolius	44.45	-121.56	13 16 19	34	0.65	0.61
YAH	Yaquina Head	44.67	-124.07	13 16 19	13	2.08	2.05
NGB	NGBER	43.47	-119.69	13 16 19	7	1.07	1.06

736

737

738

739

740

741

742

743

744

745

746

747

748

749

750 Appendix 2: Metrics computed from a posteriori covariances for regions shown in figure 1. Note

751 a posteriori cross-correlation coefficients and cross-covariances have also been shown in figure 2.

752 Correlation coefficients shown in figure 2 are computed by dividing the a posteriori cross-
 753 covariances by the product of a posteriori standard deviations of the biospheric and fossil fuel
 754 fluxes.

755

I. A posteriori correlation coefficient between biospheric and fossil fuel fluxes			
	RD1	RD2	SD
Northeast	-0.55	-0.56	-0.19
Southeast	-0.35	-0.48	-0.19
Midwest	-0.58	-0.66	-0.24
South central	-0.44	-0.55	-0.16
II. A posteriori cross covariance between biospheric and fossil fuel fluxes ($\mu\text{mol m}^{-2}\text{sec}^{-1}$)²			
	RD1	RD2	SD
Northeast	-0.012	-0.026	-0.005
Southeast	-0.005	-0.017	-0.004
Midwest	-0.005	-0.014	-0.005
South central	-0.002	-0.006	-0.001
III. A posteriori standard deviation of fossil fuel fluxes ($\mu\text{mol m}^{-2}\text{sec}^{-1}$)			
	RD1	RD2	SD
Northeast	0.132	0.231	0.103
Southeast	0.092	0.176	0.103
Midwest	0.087	0.155	0.092
South central	0.054	0.098	0.044

IV. A posteriori standard deviation of biospheric fluxes ($\mu\text{mol m}^{-2}\text{sec}^{-1}$)			
	RD1	RD2	SD
Northeast	0.171	0.197	0.240
Southeast	0.166	0.197	0.222
Midwest	0.109	0.136	0.220
South central	0.097	0.115	0.201

756

757

758

759

760

761

762

763

764 Appendix 3: Estimates of error covariance parameters for (a) biospheric (\mathbf{Q}_{bio}), and (b) fossil fuel
 765 \mathbf{Q}_{ff} error covariance matrices. Note only results for the fossil fuel covariance structure that
 766 minimized BIC (see Table 1) are shown. Estimates for \mathbf{Q}_{bio} covariance parameters for three case
 767 studies

768 (a) Estimates for \mathbf{Q}_{bio} covariance parameters for three case studies

Case Studies	σ ($\mu\text{mol m}^{-2}\text{sec}^{-1}$)	$l_{temporal_{bio}}$ (days)	$l_{spatial_{bio}}$ (Km)
RD1	5.15	2.69	400
RD2	5.71	3.20	383
SD	0.21	5.28	1204

769 (b) Estimates for \mathbf{Q}_{ff} covariance parameters for three case studies

Case Studies	a ($\mu\text{mol m}^{-2}\text{sec}^{-1}$)	b (unitless)
RD1	0.02	8.69E-08
RD2	2.33	4.62E-13
SD	1.01E-06	6.0E-03

770

771

772

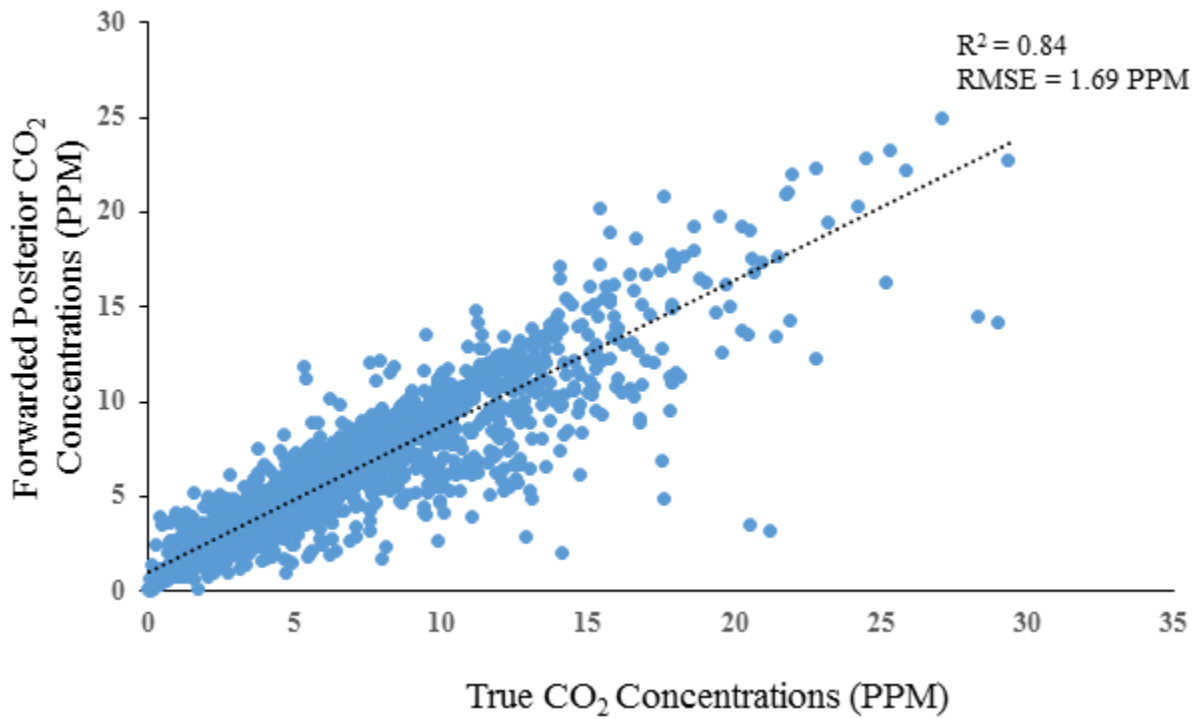
773

774

775 Appendix 4: Scatterplot of true and posterior concentration fits for (a) RD1, and (b) RD2 case
776 studies. Note these figure shown results after removing the influence of boundary conditions.RD1
777 case study

778

779 (a) RD1 case study



780

781

782

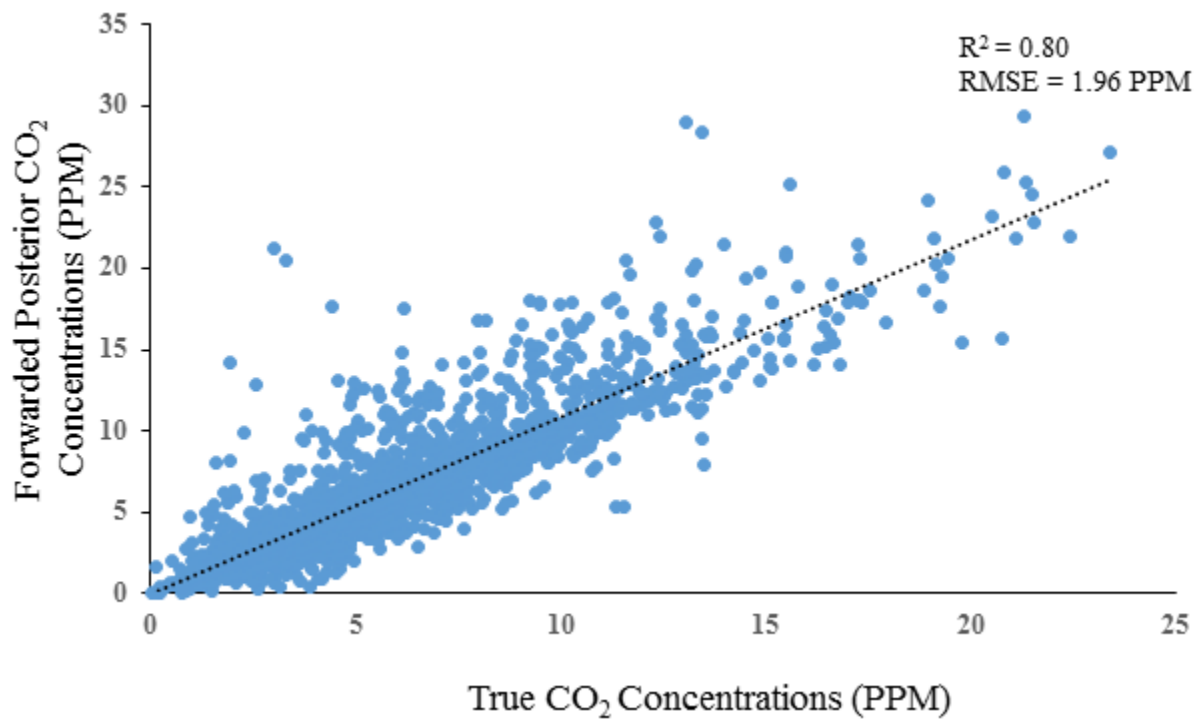
783

784

785

786

787 (b) RD2 case study



788

789